A&A 583, A56 (2015)
DOI: 10.1051/0004-6361/201526743

Astronomy & Astrophysics

Chemical abundance study of two strongly *s*-process enriched post-AGB stars in the LMC: J051213.81-693537.1 and J051848.86-700246.9⋆,⋆⋆

K. De Smedt[1], H. Van Winckel[1], D. Kamath[1], and P. R. Wood[2]

[1] Instituut voor Sterrenkunde, K.U. Leuven, Celestijnenlaan 200D, 3001 Leuven, Belgium
e-mail: kenneth.desmedt@ster.kuleuven.be
[2] Research School of Astronomy and Astrophysics, Mount Stromlo Observatory, Weston Creek ACT 2611, Australia

Received 15 June 2015 / Accepted 9 July 2015

ABSTRACT

Context. This paper is part of a larger project in which we systematically study the chemical abundances of extra-galactic post-asymptotic giant branch (post-AGB) stars. The aim of our programme is to derive chemical abundances of stars covering a large range in luminosity and metallicity with the ultimate goal of testing, constraining, and improving our knowledge of the poorly understood AGB phase, especially the third dredge-up mixing processes and associated *s*-process nucleosynthesis.
Aims. Post-AGB photospheres are dominated by atomic lines and indicate the effects of internal chemical enrichment processes over the entire stellar lifetime. In this paper, we study two carefully selected post-AGB stars: J051213.81-693537.1 and J051848.86-700246.9 in the Large Magellanic Cloud (LMC). Both objects show signs of *s*-process enhancement. The combination of favourable atmospheric parameters for detailed abundance studies and their known distances (and hence luminosities and initial masses) make these objects ideal probes of the AGB third dredge-up and *s*-process nucleosynthesis in that they provide observational constraints for theoretical AGB models.
Methods. We use high-resolution optical UVES spectra to determine accurate stellar parameters and subsequently perform detailed elemental abundance studies of post-AGB stars. Additionally, we use available photometric data covering optical and IR bands to construct spectral energy distributions for reddening and luminosity determinations. We then estimate initial masses from theoretical post-AGB tracks.
Results. We obtained accurate atmospheric parameters for J051213.81-693537.1 ($T_{\rm eff}$ = 5875 ± 125 K, log g = 1.00 ± 0.25 dex, [Fe/H] = −0.56 ± 0.16 dex) and J051848.86-700246.9 ($T_{\rm eff}$ = 6000 ± 125 K, log g = 0.50 ± 0.25 dex, [Fe/H] = −1.06 ± 0.17 dex). Both stars show extreme *s*-process enrichment associated with relatively low C/O ratios of 1.26 ± 0.40 and 1.29 ± 0.30 for J051213-693537.1 and J051848-700246.9, respectively. We could only derive upper limits of the lead (Pb) abundance. These upper limits show a possible very slight Pb overabundance with respect to heavy *s*-elements for J051213-693537.1, while J051848-700246.9 shows an upper limit of the Pb abundance similar to [hs/Fe]. A comparison with theoretical post-AGB evolutionary tracks in the HR-diagram reveals that both stars have low initial masses between 1.0 and 1.5 $M_{\odot}$.
Conclusions. This study adds to the results obtained so far on a very limited number of *s*-process enriched stars in the Magellanic Clouds. With the addition of the two stars in this study, we find an increasing discrepancy between observed and predicted Pb abundances towards lower metallicities of the studied *s*-process rich post-AGB stars in the Magellanic Clouds. The more metal-rich J051213-693537.1 fits the theoretical Pb abundance predictions well, while the five other objects with [Fe/H] < 1, including J051848-700246.9, have much lower Pb overabundances than predicted. In all objects found so far, including the objects in this study, the C/O ratio is very moderate because of the enhancement of O as well as C. We find that all *s*-process rich stars in the LMC and SMC studied so far, cluster in the same region of the HR-diagram and are associated with low-mass stars with a low metallicity on average. We corroborate the published lack of correlation between the metallicity and the neutron irradiation, while the neutron exposure ([hs/ls]) is strongly correlated with the third dredge-up efficiency ([s/Fe]). These correlations seem to hold in our Galaxy as well as in the Magellanic Clouds.

Key words. stars: AGB and post-AGB – stars: abundances – stars: evolution – Magellanic Clouds

1. Introduction

Post-asymptotic giant branch (post-AGB) stars are low- to intermediate-mass stars ($M \leqslant 8\ M_{\odot}$) in a transient evolutionary phase between the AGB and the white dwarf (WD) phase. In single stars, a superwind mass loss terminates the AGB phase after which the star evolves onto the post-AGB phase, eventually cooling down as a white dwarf. During the AGB phase, the end products of internal chemical processes like C, N, O and *s*-process elements are transported to the stellar surface by multiple dredge-up events, called the third dredge-up (TDU). The *s*-process synthesis in AGB stars is an important contributor to the cosmic abundances past the iron peak and these stars are also expected to be important contributors to the cosmic carbon and nitrogen enrichment (e.g Romano et al. 2010; Kobayashi et al. 2011).

⋆ Based on observations collected with the Very Large Telescope at the ESO Paranal Observatory (Chili) of programme number 088.D-0433.
⋆⋆ Atomic data are only available at the CDS via anonymous ftp to cdsarc.u-strasbg.fr (130.79.128.5) or via http://cdsarc.u-strasbg.fr/viz-bin/qcat?J/A+A/583/A56

Photospheric spectra of AGB stars are dominated by molecular bands and they are often veiled by circumstellar dust, making it difficult to study abundances of individual elements (e.g. Abia et al. 2008). However, post-AGB spectra are dominated by atomic transitions, allowing extensive abundance studies of individual elements. Their photospheres bear witness to the total chemical changes accumulated during the stellar lifetime, making them ideal tracers for the study of AGB nucleosynthesis and associated TDUs.

Chemical studies of Galactic post-AGB stars show a large variety of chemical abundance patterns (e.g. Van Winckel 2003, and references therein). Only about 25% of the studied Galactic post-AGB stars indicate strong *s*-process enrichment (e.g. Rao et al. 2012, and references therein). Although stars in the Galactic sample of post-AGB stars are well studied, their unknown distances hamper accurate luminosity determinations and hence accurate initial mass estimates, which are a key parameter in constraining single star evolution and nucleosynthesis AGB models.

One way to overcome this distance problem, is to study post-AGB stars in the Magellanic Clouds. The distances to the Magellanic Clouds are well known, with the LMC at a distance of about 50 kpc (Keller & Wood 2006; Reid & Parker 2010; Storm et al. 2011) and the SMC at a distance of about 60 kpc (Keller & Wood 2006). Furthermore, the Magellanic Cloud stars generally have lower mean metallicities than their Galactic counterparts, with a mean metallicity of ~ -0.5 dex for the LMC (e.g. Geisler et al. 2009; Lapenna et al. 2012) and ~ -0.7 dex for the SMC (Luck et al. 1998). This allows for the study of post-AGB stars in a broad metallicity range.

Therefore, we initiated a larger project in which we search for post-AGB stars in the Magellanic Clouds and then use these objects to study the poorly understood AGB TDUs and *s*-process nucleosynthesis. van Aarle et al. (2011) and Kamath et al. (2015), provide catalogues of spectroscopically verified optically visible post-AGB candidates in the Large Magellanic Cloud (LMC) and Kamath et al. (2014) provides a catalogue of spectroscopically verified optically visible post-AGB candidates in the Small Magellanic Cloud (SMC).

In this paper, we present the detailed chemical study of two newly identified LMC post-AGB candidates that were carefully selected (based on their stellar parameters and spectral features) from our optically visible post-AGB LMC catalogues.

Our previous abundance studies of strongly *s*-process enriched post-AGB stars in the Magellanic Clouds by De Smedt et al. (2012), van Aarle et al. (2013), and De Smedt et al. (2014) show that there are still large discrepancies between observed abundances and theoretical predictions. The biggest discrepancies are related to the C/O ratio since observationally derived C/O ratios are small in comparison to the theoretical predictions. The theoretical carbon abundance is often overestimated, whereas the derived oxygen abundance is larger than predicted. Also lead (Pb, $Z = 82$), which is considered to be the end product of the *s*-process chain due to its double magic number, is strongly overestimated by theoretical models as shown in De Smedt et al. (2014).

We describe the observations and data reduction of both objects in Sect. 2. Detailed abundance analysis of the obtained spectra is presented in Sect. 3 followed by the discussion of the abundances in Sect. 4. Luminosity determinations and initial mass estimates are presented in 5. We discuss the neutron irradiation of our sample stars in Sect. 6. Finally, we end with a brief discussion and conclusions in Sect. 7.

Table 1. Overview of observations.

Object name (IRAC)	Exp. time (s) Blue arm	Exp. time (s) Red arm	*V* mag
J051213.81-693537.1	6×1500	6×1500	15.7
J051848.86-700246.8	1×1500	2×1500	15.5

Notes. Exp. time represents the exposure time. The red arm is the combination of the lower and upper part of the mosaic CCD chip. The parameter *V* represents the visual magnitude.

2. Observations and data reduction

We obtained high-resolution spectra using the UVES echelle spectrograph (Dekker et al. 2000) mounted on the 8 m UT2 Kueyen Telescope of the VLT array at the Paranal Observatory of ESO in Chili. We selected the dichroic beam-splitter resulting in a wavelength coverage for the blue arm from approximately 3280 to 4530 Å, and in the red arm for the lower and upper part of the mosaic CCD chip from approximately 4780 to 5770 Å and from 5800 to 6810 Å, respectively. A slit width of 1 arcsec was used as a compromise between spectral resolution and slit-loss minimalisation. An overview of the observations is given in Table 1. For J051848.86-700246.8 (hereafter abbreviated to J051848), only one blue spectrum was available because of an instrumental error. For J051213.81-693537.1 (hereafter abbreviated to J051213), two additional spectra were also obtained but because of the significant lower quality with respect to the six other spectra, these two spectra are not used for this study. The spectra of each object were obtained in one night and in one large time interval.

The data was reduced using the UVES pipeline (version 5.3.0) in the Reflex environment of ESO[1]. This reduction includes the standard steps of extracting frames, determining wavelength calibration, applying this scale to flat-field divided data and cosmic-clipping. The standard reduction parameters of the UVES pipeline were used as these gave the best signal-to-noise (S/N) of the final spectra.

After reduction, weighted mean spectra were calculated for the three wavelength ranges. Since all spectra were taken in small time intervals, no velocity corrections were needed for calculating the weighted mean. These weighted mean spectra were then divided into subspectra, each with a fixed wavelength range of 120 Å for which the first and last 10 Å overlapped with the previous and subsequent spectra. Each of these subspectra was normalised individually by fitting fifth order polynomials through interactively defined continuum points. All subspectra were then again merged into one large spectrum, which is used for the spectral analysis. In the wavelength regions where the subspectra overlapped, the mean flux was calculated.

The wavelength range from 3280 to about 3900 Å has a poor S/N, making it unsuitable for accurate spectral analysis. We therefore did not use this spectral region in the analysis. The mean S/N in the remaining wavelength range of the blue spectrum is about 25 for both stars. The red spectra have a higher mean S/N between 80 and 100. The high resolution of the UVES spectra permits accurate radial velocity determinations using the positions of spectral lines. Line positions are measured by fitting a Gaussian through the measured line profiles, line identification is based upon the rest wavelengths from the VALD database Kupka et al. (1999). We find a radial velocity of 227.8 ± 1.9 km s^{-1} for J051848 and a radial velocity of

[1] https://www.eso.org/sci/software/reflex/

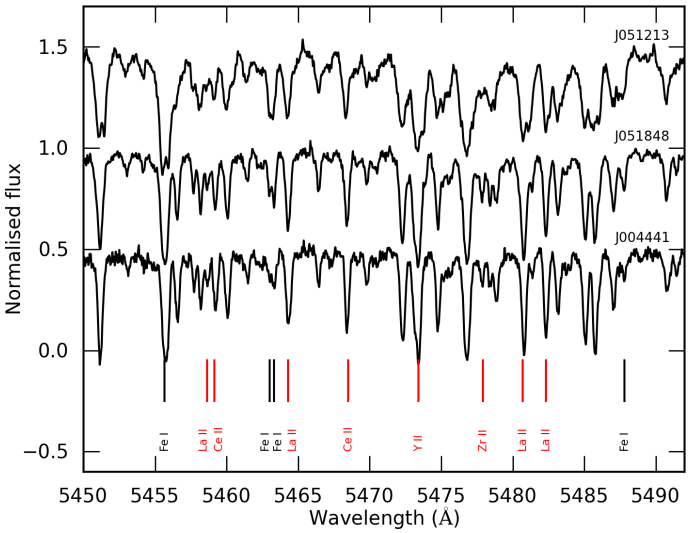

Fig. 1. Comparison of the normalised spectra of J051213 (*upper*), J051848 (*middle*), and J004441 (*lower*). The upper and lower spectra have been shifted in flux for clarity and all spectra are shifted to a zero velocity. Red and black vertical lines mark positions of *s*-nuclei and non *s*-nuclei, respectively. See text for more information.

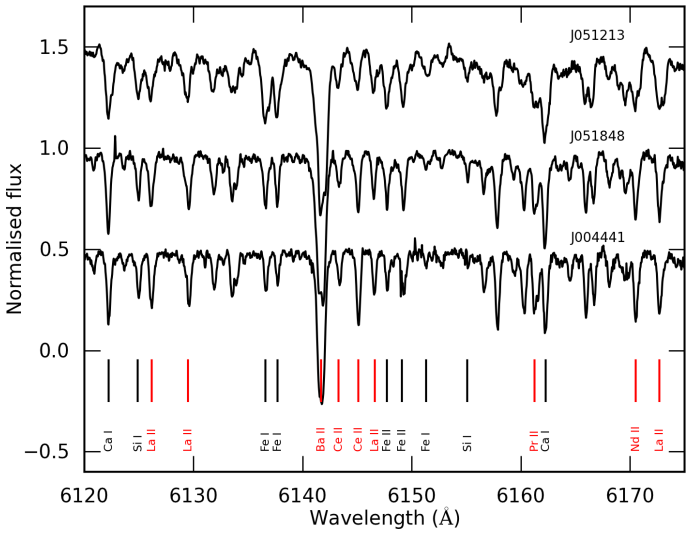

Fig. 2. Similar to Fig. 1, except for another wavelength range.

284.3 ± 1.0 km s^{-1} for J051213. Both radial velocities are consistent with the average radial velocity of the LMC, which is approximately 270 km s^{-1} (van der Marel et al. 2002).

3. Spectral analyses

A visual inspection of the UVES spectra immediately shows the very strong *s*-process enrichment for both objects. Figures 1 and 2 show different wavelength regions of J051213 and J051848. Both figures also show the corresponding spectral region of J004441.04-732136.4 (J004441), which is a strongly *s*-process enhanced SMC post-AGB star (De Smedt et al. 2012). All three objects have similar atmospheric parameters except for the metallicity as described in Sect. 3.1. Both J051213 and J051848 show strong Ba II (Fig. 2) and Y II (Fig. 1) lines, which is a clear indication of *s*-process enrichment. Although J051213 and J051848 are members of the LMC, while J004441 is an SMC object, they have similar spectra.

The spectral analyses includes atmospheric parameter and abundance determination. We use PyMOOG, our own Python wrapper around the local thermal equilibrium (LTE) abundance calculation routine MOOG (version June 2014 Sneden 1973). For the analyses of our two LMC stars, we use the LTE Kurucz-Castelli atmosphere models (Castelli & Kurucz 2003). As with the radial-velocity determination, spectral lines are identified using linelists from the VALD database (Kupka et al. 1999). We combine the VALD line-lists with a list of lines gathered at the Instituut voor Sterrenkunde for the chemical analysis of A, F, and G stars (Van Winckel & Reyniers 2000). The line-lists implemented in PyMOOG cover a wavelength range from 3000 up 11 000 Å. This covers the full wavelength coverage of the UVES spectra, and allows for the identification of spectral lines of about 160 ions ranging from He (Z = 2) up to U (Z = 92). We included neutral and firstly-ionised ions for most of the elements. For some *s*-process elements, the second ionisation is included although the effective temperatures of the two sample stars in this study are too low for these ionisations.

The equivalent width (EW) of spectral lines are measured interactively with PyMOOG. The EWs are calculated with direct integration. The abundances are computed with an iterative process in which the theoretical EWs of single lines are computed for given abundances and matched to the observational EWs. For our analysis, we avoided blended lines as much as possible. Synthetic spectra were used for checking whether used spectral lines are part of blends with other identified lines.

3.1. Atmospheric parameters

The atmospheric parameters are determined using the atmospheric parameter determination module in PyMOOG. We use linear interpolation to calculate atmospheric models, which are within the parameter steps of the Kurucz-Castelli models. For the determination of the effective temperature and surface gravity $\log g$, we use parameter steps of 125 K and 0.5 dex, respectively. For the microturbulent velocity, we choose steps of 0.2 km s^{-1}.

To derive the atmospheric parameters, we use Fe I and Fe II lines. The effective temperature $T_{\rm eff}$ is determined by enforcing the iron abundance, derived from the individual Fe I lines, to be independent of lower excitation potential. We choose Fe I lines for this purpose since the available Fe II lines do not cover an appropriate range in lower excitation potential. The surface gravity $\log g$ is determined by enforcing ionisation equilibrium between the individual Fe I and Fe II abundances. The microturbulent velocity ξ_t is derived by enforcing the iron abundance from individual Fe I lines to be independent of reduced equivalent width, which we define in this contribution as EW/λ.

The individual atmospheric parameter results together with the number of used individual spectral lines are shown in Table 2. The indicated uncertainties of [FeI/H] and [FeII/H] are the total errors on the iron abundances, which includes line-to-line scatter and the atmospheric parameter uncertainties as described below in Sect. 3.2. The metallicity of J051213 is similar to the mean LMC metallicity of −0.4 dex, while J051848 has a significantly lower metallicity.

Both stars are of spectral type F and have low surface gravities confirming their evolved nature. The effective temperatures of both stars could be determined accurately. Kamath et al. (2015) estimate stellar parameter for J051848, based on low-resolution spectra. We find that the derived stellar parameters

Table 2. Determined atmospheric parameters of J051213 and J051848.

Object	J051213	J051848
$T_{\rm eff}$ (K)	5875 ± 125	6000 ± 125
$\log g$ (dex)	1.00 ± 0.25	0.50 ± 0.25
ξ_t (km s^{-1})	3.0 ± 0.2	2.8 ± 0.2
[FeI/H]	–0.56 ± 0.16	–1.06 ± 0.17
[FeII/H]	–0.56 ± 0.15	–1.03 ± 0.14
$N_{\rm FeI}$	53	35
$N_{\rm FeII}$	13	9

Notes. The errors for [Fe/H] include line-to-line scatter and model uncertainty. Symbols $N_{\rm FeI}$ and $N_{\rm FeII}$ show the number of lines used for Fe I and Fe II, respectively.

of our study and those of Kamath et al. (2015) agree well within the estimated errors.

3.2. Abundance determination

We use the derived atmospheric parameters in Table 2 for the abundance determination using PyMOOG. We mainly use isolated non-blended, non-saturated lines, but this is a challenge because of the rich spectra with strong enhancements. However, with spectral synthesis, we determine the abundances of ions, which can only be found in blends. Lines with EWs smaller than 5 mÅ are not used as they may be confused with noise in the spectra.

Only a few carbon and oxygen lines are available for abundance determination because most of the lines are severely blended. For J051213, where only one spectral line was available for both the C and O abundances, these abundances were determined using spectral synthesis. The O abundance of J051213 is determined using the forbidden [O I] line at 6300 Å, which is part of a fully identified blend. This line is not sensitive to non-LTE effects (e.g. Kiselman 2002). For J051848, we found four useful lines for carbon and two non-forbidden O I lines. For both stars, nitrogen lines larger than 5 mÅ are not found in the available wavelength coverage of the UVES spectra.

The spectra of both objects allowed abundance determinations of many elements past the iron peak. Unfortunately, all available Sr and Ba lines are heavily saturated hampering accurate abundance determinations for these two *s*-process elements. Most of the other studied *s*-elements abundances are determined from multiple, single lines. Apart from the light *s*-process (ls) peak elements Y and Zr, and heavy *s*-process (hs) peak elements La, Ce, Pr, and Nd, we find abundances for heavier elements like gadolinium (Gd, $Z = 64$), dysprosium (Dy, $Z = 66$), erbium (Er, $Z = 68$), thulium (Tm, $Z = 69$), luthetium (Lu, $Z = 71$), and hafnium (Hf, $Z = 72$).

To illustrate our analyses, in Fig. 3 we show the comparison between synthetic spectra with different Nd abundances for J051213 around the Nd II line at 6727.695 Å. The red line represents the best synthetic fit to the observations. The figure shows that our derived abundances reproduce well the observed spectral lines. A similar fit for the Eu II line at 6645.064 Å for J051848 is shown in Fig. 4.

Lead (Pb, $Z = 82$) is a very important tracer of the *s*-process nucleosynthesis. Unfortunately, at the photospheric conditions of our stars, the useful Pb lines are in the very blue part of the spectrum. Because of the low S/N around the strongest Pb I line at 4057.807 Å, it is difficult to determine accurate Pb abundances for both sample stars, therefore, we prefer to determine Pb abundance upper limits. For J051213, the S/N is poor as can be seen in Fig. 5. The combination of many unidentified spectral lines, i.e. lines not included in the line-lists, and the poor S/N make it difficult to determine the position of the continuum. For some unidentified lines, we mark the positions indicated with question marks. For J051848, the S/N is higher, but again many unidentified lines are present in the spectral region

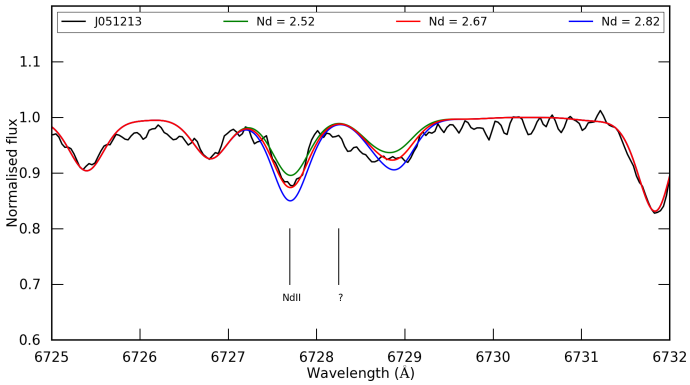

Fig. 3. Spectrum synthesis of the Nd II line at 6727.695 Å for J051213. The black spectrum is the observed spectrum, the coloured spectra represent synthetic spectra with different Nd abundances. The position of the Nd line is indicated. For more information, see text.

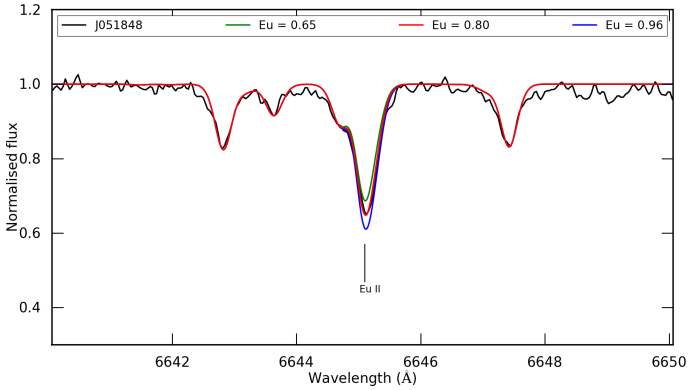

Fig. 4. Spectrum synthesis of the Eu II line at 6645.064 Å for J051848. The black spectrum is the observed spectrum, the coloured spectra represent synthetic spectra with different Eu abundances. The position of the Eu line is indicated. For more information, see text.

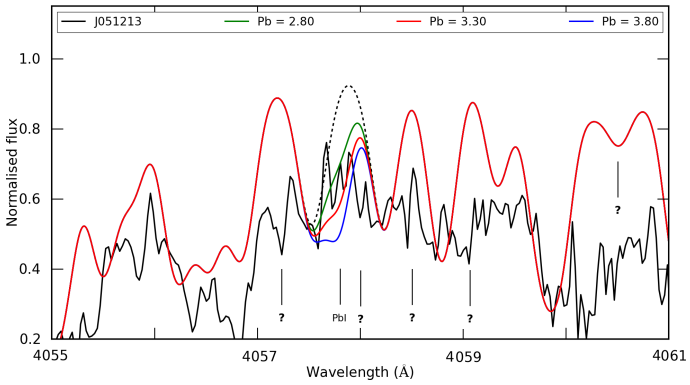

Fig. 5. Spectrum synthesis of the Pb I line at 4057.807 Å for J051213. The black spectrum is the observed spectrum of J051213, the coloured spectra represent synthetic spectra with different Pb abundances. The dashed black line shows the synthetic spectrum if no Pb is present. Positions of unidentified spectral lines are indicated by question marks. For more information, see text.

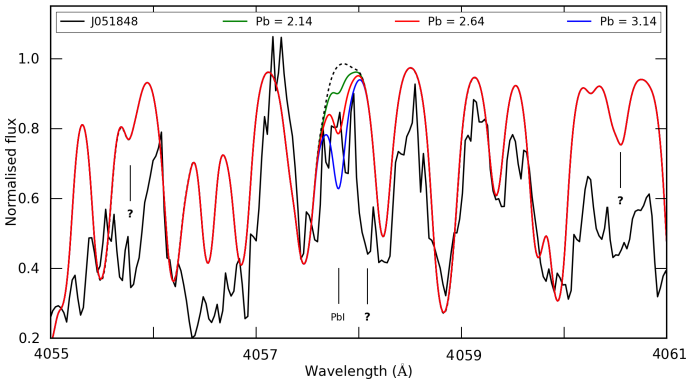

Fig. 6. Spectrum synthesis of the Pb I line at 4057.807 Å for J051848. The black spectrum is the observed spectrum, the coloured spectra represent synthetic spectra with different Pb abundances. The dashed black line shows the synthetic spectrum if no Pb is present. Positions of unidentified spectral lines are indicated by question marks. For more information, see text.

(as shown in Fig. 6). For both stars, we use the spectral blended lines at 4057.5, 4058.3, 4058.8, and 4059.9 Å to estimate the position of the continuum at the Pb I line by eye. With our adopted local continuum positions, small Pb line features are present in the observed spectra as the dashed lines represent synthetic spectra without the Pb I line at 4057.807 Å.

4. Abundance results

The complete abundance analysis results of both objects are presented in Tables 3 and 4. An overview of the lines used for these analyses can be found in two catalogues, which are available at CDS. The information in each catalogue is tabulated as follows: Col. 1 lists the name of the ion to which the corresponding line belongs, Col. 2 shows the rest wavelength, Col. 3 contains the lower excitation potential, Col. 4 mentions the logarithm of the oscillator strength, Col. 5 lists the measured EW, and Col. 6 gives the deduced abundance for the corresponding line.

Based upon the ionisation potential of the corresponding ion, the element over iron ratios ([X/Fe]) in Tables 3 and 4 are calculated using Fe I or Fe II. If the ionisation potential of an ion is below the ionisation potential of Fe I, the abundance of Fe I is used for calculating [X/Fe]. If the ionisation potential exceeds the ionisation potential of Fe I, Fe II is used for calculating [X/Fe]. The same principle is also used for calculating the total error of [X/Fe]. The errors were determined using the method described in Deroo et al. (2005). The uncertainties due to the atmospheric parameters are calculated by determining the abundances of a certain ion for atmospheric models with $T_{\rm eff}$ plus and minus 125 K, models with $\log g$ plus and minus 0.25 dex and microturbulent velocity plus and minus 0.2 km s^{-1} (see Table 2). The uncertainty in microturbulent velocity can have important effects for ions, which are only determined by large lines like Y II. The total uncertainties are then the quadratic sum of the uncertainties of the mean due to line-to-line scatter ($\sigma_{\rm l2l}$), uncertainties due to atmospheric parameters ($\sigma_{T_{\rm eff}}$, $\sigma_{\log g}$, σ_{ξ_t}), and the Fe abundance uncertainty ($\sigma_{\rm Fe}$):

$$\sigma_{\rm tot} = \sqrt{\left(\frac{\sigma_{\rm l2l}}{\sqrt{N_{\rm ion}}}\right)^2 + (\sigma_{T_{\rm eff}})^2 + (\sigma_{\log g})^2 + (\sigma_{\xi_t})^2 + \left(\frac{\sigma_{\rm Fe}}{\sqrt{N_{\rm Fe}}}\right)^2}.$$

The scaling to Fe I or Fe II based upon ionisation potential strongly decreases the [X/Fe] uncertainty of certain ions with respect to using only Fe I or only Fe II for all [X/Fe] calculations.

Table 3. Abundance results of J051213.81-693537.1.

	J051213					Sun
	$T_{\rm eff}$ = 5875 K			ξ_t = 3.0 km s^{-1}		
	$\log g$ = 1.00 dex			[Fe/H] = −0.56 dex		
Ion	N	$\log \epsilon$	$\sigma_{\rm l2l}$	[X/Fe]	$\sigma_{\rm tot}$	$\log \epsilon_\odot$
C I	1	8.75	0.20	0.88	0.26	8.43
O I	1	8.65	0.20	0.52	0.26	8.69
Mg I	1	7.00	0.20	–0.04	0.24	7.60
Al I	1	6.60	0.20	0.71	0.25	6.45
Si I	4	7.32	0.05	0.37	0.18	7.51
S I	2	6.51	0.03	–0.05	0.13	7.12
Ca I	11	6.00	0.09	0.22	0.09	6.34
Ca II	1	6.00	0.20	0.22	0.24	6.34
Sc II	3	2.93	0.03	0.34	0.10	3.15
Ti I	2	4.69	0.07	0.30	0.13	4.95
Ti II	7	4.62	0.13	0.23	0.11	4.95
V I	1	3.91	0.20	0.54	0.25	3.93
V II	2	3.91	0.04	0.54	0.14	3.93
Cr I	4	5.20	0.07	0.12	0.10	5.64
Cr II	7	5.16	0.11	0.08	0.10	5.64
Mn I	1	4.69	0.20	–0.18	0.24	5.43
Fe I	53	6.94	0.10	0.00	0.06	7.50
Fe II	13	6.94	0.09	0.00	0.07	7.50
Ni I	4	5.75	0.08	0.09	0.12	6.22
Zn I	1	4.22	0.20	0.22	0.29	4.56
Y II	5	3.13	0.11	1.48	0.13	2.21
Zr II	2	3.20	0.02	1.18	0.10	2.58
La II	6	2.52	0.13	1.98	0.13	1.10
Ce II	6	2.91	0.12	1.89	0.13	1.58
Pr II	6	1.96	0.06	1.80	0.13	0.72
Nd II	14	2.67	0.10	1.81	0.13	1.42
Sm II	1	1.70	0.20	1.30	0.24	0.96
Eu II	2	0.98	0.07	1.02	0.13	0.52
Dy II	2	2.00	0.20	1.46	0.21	1.10
Er II	2	1.90	0.20	1.54	0.22	0.92
Pb I^u	1	3.30	0.20	2.11	0.25	1.75
Th II^u	1	1.35	0.20	1.89	0.27	0.02

Notes. The table lists for each ion the used number of lines (N) for the abundance determination, the determined abundance ($\log \epsilon$), the uncertainty of this abundance due to line-to-line scatter ($\sigma_{\rm l2l}$), the element over iron ratio ([X/Fe]), and total uncertainty ($\sigma_{\rm tot}$). The total uncertainty $\sigma_{\rm tot}$ includes line-to-line scatter and atmospheric parameter uncertainty (see text for details). The last column lists the solar abundances from Asplund et al. (2009). We choose a standard deviation of 0.20 dex for all ions for which the abundance was derived using spectrum synthesis or for which only one line is available. $^{(u)}$ These abundances are upper limits.

The [X/Fe] results in Tables 3 and 4 are plotted in Figs. 7 and 8, respectively.

4.1. Carbon and oxygen

Both stars are carbon enhanced. The uncertainties of C and O for J051213 are large since only one line could be used for the abundance determinations. Both ions are also strongly sensitive to changes in effective temperature. We find [C/Fe] values of about 0.9 and 1.2 for J051213 and J051848, and [O/Fe] values of about 0.5 and 0.8. This results in moderate C/O ratios of only 1.26 ± 0.40 for J051213 and 1.29 ± 0.30 for J051848, which are a combination of relatively low C enhancements as well as relatively high O enhancements. Based upon their abundances (Figs. 7 and 8) and their luminosities (see Sect. 5), both stars are carbon-enhanced post-AGB stars but the C/O ratios are not very large.

Table 4. Abundance results for J051848.86-700246.9.

	J051848					Sun
	$T_{\rm eff}$ = 6000 K		ξ_t = 2.8 km s^{-1}			
	log g = 0.50 dex		[Fe/H] = −1.03 dex			
Ion	N	log ϵ	$\sigma_{\rm 12I}$	[X/Fe]	$\sigma_{\rm tot}$	log $\epsilon_\odot$
C I	4	8.61	0.13	1.21	0.16	8.43
O I	2	8.50	0.05	0.84	0.19	8.69
Mg I	2	6.73	0.07	0.19	0.12	7.60
S I	1	6.46	0.20	0.37	0.25	7.12
Ca I	8	5.56	0.08	0.28	0.08	6.34
Sc II	6	2.30	0.08	0.18	0.11	3.15
Ti II	4	4.12	0.08	0.20	0.11	4.95
Cr I	6	4.70	0.07	0.12	0.08	5.64
Cr II	12	4.78	0.07	0.17	0.08	5.64
Fe I	35	6.44	0.07	0.00	0.05	7.50
Fe II	9	6.47	0.12	0.00	0.10	7.50
Ni I	8	5.22	0.10	0.06	0.10	6.22
Cu I	1	3.53	0.20	0.40	0.23	4.19
Zn I	1	3.78	0.20	0.25	0.29	4.56
Y II	6	2.79	0.12	1.61	0.15	2.21
Zr II	2	2.85	0.05	1.30	0.13	2.58
La II	7	2.55	0.11	2.48	0.20	1.10
Ce II	5	2.37	0.07	1.82	0.13	1.58
Pr II	11	1.75	0.05	2.06	0.14	0.72
Nd II	14	2.69	0.10	2.30	0.16	1.42
Sm II	2	1.80	0.12	1.87	0.18	0.96
Eu II	2	0.81	0.12	1.32	0.17	0.52
Gd II	10	1.75	0.12	1.71	0.12	1.07
Dy II	4	1.91	0.09	1.84	0.12	1.10
Er II	1	1.63	0.20	1.74	0.26	0.92
Tm II	1	1.20	0.20	2.13	0.24	0.10
Lu II	3	1.16	0.08	2.08	0.15	0.10
Hf II	1	1.84	0.20	2.02	0.25	0.85
Pb I^u	1	2.62	0.20	1.93	0.25	1.75

Notes. Same as for Table 3.

4.2. α-elements

Concerning the available α-elements Mg, Si, S, Ca, and Ti, the mean of [X/Fe] is [α/Fe] = +0.14 and [α/Fe] = +0.26 for J051213 and J051848, respectively. For J051848, no Si abundance was available. With respect to Galactic abundances, these α-element abundance are slightly deficient but they fall within the expected abundance ranges for the LMC, consistent with their respective metallicities (e.g Van der Swaelmen et al. 2013; Pompéia et al. 2008).

4.3. s-process elements

The s-process elements can be subdivided into three groups. This division is based upon the number of neutrons in the nuclei. The first group is the light s-process (ls) elements around neutron magic number 50 ($Z \sim 38$) with elements like Sr, Y, and Zr. For both stars, we were only able to measure Y and Zr. The second group is the heavy s-process (hs) elements around magic neutron number 82 ($Z \sim 58$) with elements like Ba, La, Ce, Pr, Nd, and Sm. The last group consists of one element, which is the double magic ion ^{208}Pb. This has a magic neutron number of 126 and a magic proton number of 82. Because of its double magic state, ^{208}Pb is accepted as the end product of s-process nucleosynthesis.

The [X/Fe] results in Figs. 7 and 8 show strong enrichment in both stars, confirming their post third TDU status. In particular, J051848 shows strong enhancements for La (Z = 57) and Nd (Z = 60), two typical s-process elements of Ba peak. Also, the s-elements of the Sr peak are enriched, albeit less strongly then the Ba-peak elements. The abundances of elements past the hs peak are strongly enhanced in both stars.

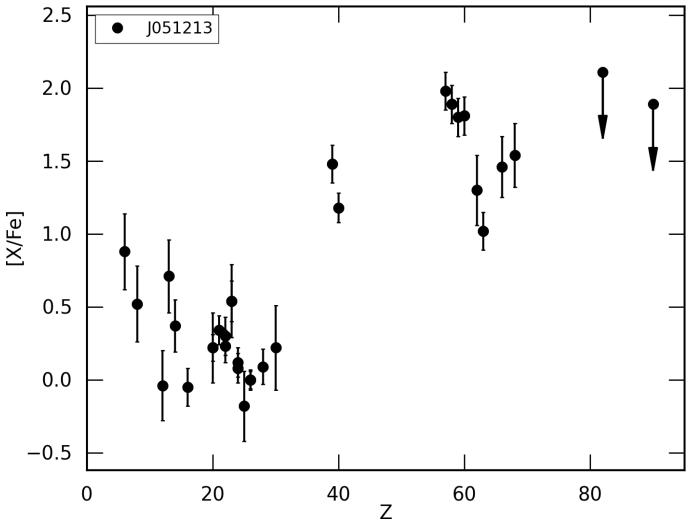

Fig. 7. [X/Fe] results of J051213. The errors bars represent the total uncertainties $\sigma_{\rm tot}$. The abundances of Pb (Z = 82) and Th (Z = 90) are upper limits and marked with down arrows.

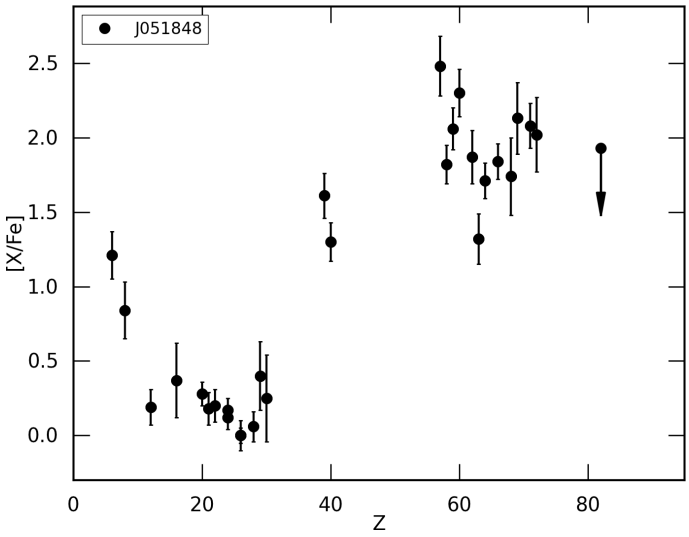

Fig. 8. [X/Fe] results of J051848. The errors bars represent the total uncertainties $\sigma_{\rm tot}$. The abundance of Pb (Z = 82) is an upper limit and marked with a down arrow.

For J051213, we find a Pb abundance upper limit that is similar to the overabundances of the Ba-peak elements. For J051848, we find that the Pb upper abundance limit is lower than the abundance ratios of La and Nd, and similar to the Ce (Z = 58) abundance ratio.

An overview of the C/O ratio, metallicity, α-element enhancement, and the observational indices used for describing s-process overabundances and distributions (see Sect. 6) are listed in Table 5.

5. Luminosity and initial mass determination

5.1. Spectral energy distributions and luminosities

The spectral energy distributions (SEDs) and known distance to the LMC allow us to determine the luminosities of our sample

Table 5. Overview of the C/O ratio, metallicity, α-element enrichment, and *s*-process indices for J051213 and J051848.

Object	C/O	[Fe/H]	[α/Fe]	[ls/Fe]	[hs/Fe]	[s/Fe]	[hs/ls]
J051213	1.26 ± 0.40	–0.56 ± 0.15	0.14 ± 0.07	1.33 ± 0.08	1.74 ± 0.08	1.61 ± 0.06	0.41 ± 0.12
J051848	1.29 ± 0.30	–1.03 ± 0.14	0.26 ± 0.08	1.46 ± 0.10	2.12 ± 0.08	1.90 ± 0.07	0.66 ± 0.13

Table 6. Estimated luminosity and reddening of J051213 and J051848.

Object	J051213	J051848
$E(B-V)$	0.69 ± 0.03	0.44 ± 0.02
$L\,(L_\odot)$	6700 ± 200	6250 ± 200

stars and estimate their initial masses (Sect. 5.2). The photometric data for constructing the SEDs are retrieved from the following catalogues: the UBVR CCD Survey of the Magellanic Clouds (Massey 2002), the 2MASS 6X catalogue (Cutri et al. 2003), the Deep Near-Infrared Survey (DENIS, Fouqué et al. 2000), the WISE All-Sky Data catalogue (Cutri et al. 2012), and the *Spitzer* SAGE survey of the LMC (Meixner et al. 2006).

For our sample post-AGB stars, we assume that three sources contribute to the reddening. The first source is reddening by interstellar dust in the Milky Way galaxy towards the LMC. Schlegel et al. (1998) find a relatively small extinction towards the LMC of $E(B-V) = 0.075$ mag. The second source is reddening by interstellar dust in the LMC. We assume similar extinction laws in the LMC and Milky Way galaxy and use the Galactic extinction curves of Cardelli et al. (1989) to determine reddening in the LMC. The third source of reddening is caused by circumstellar dust of the post-AGB object itself. We assume the circumstellar extinction has the same wavelength dependency as the Galactic extinction law.

The total dereddening is determined by applying a χ^2 minimalisation on the fit between the dereddened broadband fluxes and the appropriate Kurucz model atmospheres that are used for the abundance determination. For the scaled model of J051213, we have linearly interpolated between available models to obtain our preferred atmosphere model. The error on $E(B-V)$ is determined by a Monte Carlo simulation of 100 arrays with a normal distribution of the original flux. The luminosities are calculated by integrating the surface of the scaled Kurucz models and applying a distance of 50 kpc to the LMC (e.g. Keller & Wood 2006; Reid & Parker 2010). The errors on the luminosity are determined by a Monte Carlo simulation, similar to the error derivation of the reddening. The estimated luminosity and reddening results of both the sample stars are listed in Table 6. The constructed SEDs are shown in Figs. 9 and 10.

The SEDs in Figs. 9 and 10 are double peaked, indicating a circumstellar dust envelope originating from the strong mass-loss during the AGB (Van Winckel 2003). We find a significant reddening value for both stars; in particular, J051213 has a high line-of-sight extinction of $E(B-V) \approx 0.7$. This extinction is dominated by the circumstellar extinction given the evidence for dusty circumstellar envelopes of these objects. The derived luminosities in Table 6 are within the expected luminosity range for post-AGB stars and they agree well with the post-TDU nature of these objects.

5.2. Initial mass estimates

Two key parameters in state-of-the-art evolution and nucleosynthetic AGB models are the metallicity and initial stellar

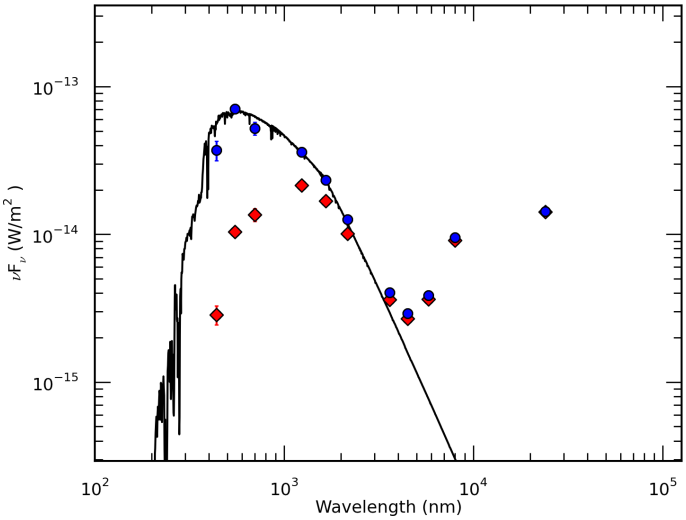

Fig. 9. SED of J051213. Red diamonds symbolise the red, original photometry, blue circles represent the dereddened photometry. The black line is the scaled Kurucz atmosphere model.

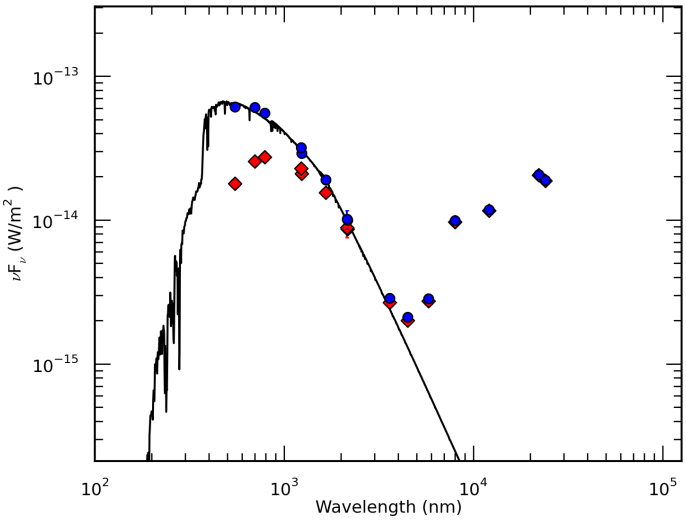

Fig. 10. SED of J051848. Symbols are identical to Fig. 9.

mass. We use the post-AGB evolutionary tracks of Vassiliadis & Wood (1994) to obtain an estimate of the initial masses of our sample stars. We compare the positions of the sample stars with those of the theoretical tracks in the Hertsprung-Russell (HR) diagram in Fig. 11. We have also included the positions of three other *s*-process enriched LMC post-AGB stars: J050632.10-714229.9, J052043.86-692341.0, and J053250.69-713925.8 (van Aarle et al. 2013), and the *s*-process enriched SMC post-AGB star J004441.04-732136.4 (De Smedt et al. 2012). For all stars, we use the theoretical tracks that were calculated for metallicity, which corresponded the most to the derived metallicities of the individual objects. The theoretical tracks from Vassiliadis & Wood (1994) start at an effective temperature of 10^4 K, which is higher than the derived temperatures

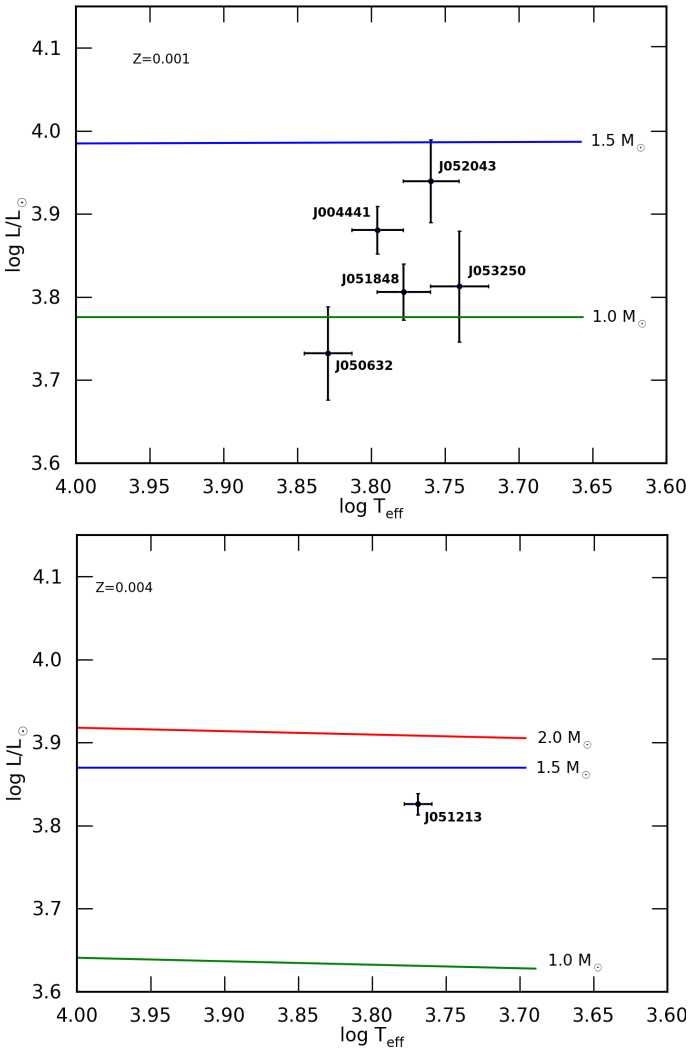

Fig. 11. Comparison of our sample stars and four other *s*-process enriched Magellanic Cloud post-AGB stars. The evolutionary tracks shown are from Vassiliadis & Wood (1994) with a metallicity of $Z = 0.001$ in the *upper panel* and $Z = 0.004$ in the *lower panel*. The mass corresponding to each track is indicated. For more information, see text.

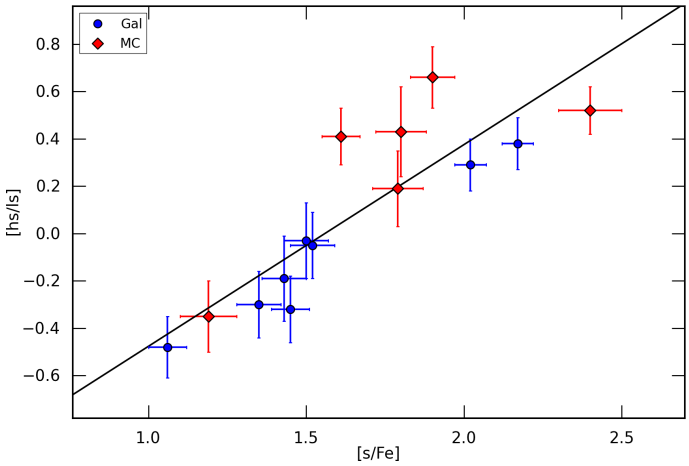

Fig. 12. Correlation between the total enrichment in *s*-process elements and the [hs/ls] index for the stars listed in 7. Galactic objects are represented by blue dots; Magellanic Cloud objects are represented by red diamonds. The full line shows the least-squares fit to all data points.

of the shown stars. Since the luminosity of post-AGB stars remains approximately constant when crossing the HR-diagram, we have used linear extrapolation between $\log T_{\rm eff}$ and $\log L/L_{\odot}$ to extrapolate towards lower temperatures.

We find that the *s*-process enriched post-AGB stars included in Fig. 11 have low masses below about 1.5 $M_{\odot}$. We find that strong *s*-process enrichment is linked to low initial masses in all sources studied so far (De Smedt et al. 2012; van Aarle et al. 2013).

We remark that our initial mass estimates depend on the applied mass-loss rate history on the AGB, and the theoretical post-AGB tracks of Vassiliadis & Wood (1994) used for the initial mass estimates, are determined using initial-final mass relations deduced at that time.

6. Neutron irradiation

The *s*-process distributions and *s*-process overabundances are typically represented by four observational indices: [ls/Fe], [hs/Fe], [s/Fe], and [hs/ls]. Unfortunately, the elemental abundances used for the calculations of these indices vary in the literature. To have a significant statistical sample, we include the abundance results from Van Winckel & Reyniers (2000) and Reyniers et al. (2004) for Galactic objects in the *s*-process index study. For the ls-index, we follow the suggestion from Busso et al. (1995) and use the mean of the relative abundances of Y and Zr. For the hs-index, normally the Ba abundance is used, but since an accurate Ba abundance study is hampered by the strong saturated Ba lines in *s*-process enriched objects, we replace the Ba abundance by the Ce abundance, which can be determined accurately in enriched objects. The hs-index is then the mean of the relative abundances of La, Ce, Nd and Sm. Our four *s*-process indices are

$$[\mathrm{ls/Fe}] = \frac{[\mathrm{Y/Fe}] + [\mathrm{Zr/Fe}]}{2};$$

$$[\mathrm{hs/Fe}] = \frac{[\mathrm{La/Fe}] + [\mathrm{Ce/Fe}] + [\mathrm{Nd/Fe}] + [\mathrm{Sm/Fe}]}{4};$$

$$[\mathrm{s/Fe}] = \frac{[\mathrm{Y/Fe}]+[\mathrm{Zr/Fe}]+[\mathrm{La/Fe}]+[\mathrm{Ce/Fe}]+[\mathrm{Nd/Fe}]+[\mathrm{Sm/Fe}]}{6};$$

$$[\mathrm{hs/ls}] = [\mathrm{hs/Fe}] - [\mathrm{ls/Fe}].$$

Since we use a non-standard element selection for the hs index calculations, we list the four *s*-process indices of all stars in our *s*-process indices analysis in Table 7. This includes Galactic object from Van Winckel & Reyniers (2000) and Reyniers et al. (2004), and Magellanic Cloud objects from this paper, De Smedt et al. (2012), and van Aarle et al. (2013). For objects IRAS 04296+3429, IRAS 19500-1709, and J053250.69-713925.8, no Sm abundance could be determined. To estimate the Sm abundance for these objects, we scale the abundance of Sm to the abundance of Nd, which is the element with an atomic mass closest to Sm and is included in the hs index. We use the AGB nucleosynthesis models from the online-database FRUITY[2] (Franec Repository of Upgraded Isotopic Tables and Yields Cristallo et al. 2011) and use the models with metallicities closest to the respective star's metallicity. We choose a standard mass of 1.5 $M_{\odot}$ based upon our estimated initial mass results for the Magellanic Cloud objects (see Sect. 5.2)

Van Winckel & Reyniers (2000), Reyniers et al. (2004), and van Aarle et al. (2013) find a strong correlation between

[2] http://fruity.oa-teramo.inaf.it/

Table 7. Overview of the four *s*-process indices of the stars in Figs. 12 and 13.

Object	[Fe/H]	C/O	[ls/Fe]	[hs/Fe]	[s/Fe]	[hs/ls]
IRAS 04296+3429[a]	–0.62 ± 0.20		1.66 ± 0.12	1.34 ± 0.07	1.45 ± 0.06	–0.32 ± 0.14
IRAS 05341+0852[a]	–0.85 ± 0.20	1.4 ± 0.3	1.92 ± 0.08	2.30 ± 0.07	2.17 ± 0.05	0.38 ± 0.11
IRAS 06530-0213[b]	–0.46 ± 0.20	2.8 ± 0.3	1.82 ± 0.09	2.11 ± 0.07	2.02 ± 0.05	0.29 ± 0.11
IRAS 07134+1005[a]	–1.00 ± 0.20	1.0 ± 0.3	1.55 ± 0.17	1.36 ± 0.07	1.43 ± 0.07	–0.19 ± 0.18
IRAS 08143-4406[b]	–0.39 ± 0.20	1.3 ± 0.3	1.52 ± 0.15	1.49 ± 0.07	1.50 ± 0.07	–0.03 ± 0.16
IRAS 19500-1709[a]	–0.60 ± 0.20	1.1 ± 0.3	1.38 ± 0.11	0.90 ± 0.07	1.06 ± 0.06	–0.48 ± 0.13
IRAS 22223+4327[a]	–0.31 ± 0.20	1.2 ± 0.3	1.55 ± 0.10	1.25 ± 0.09	1.35 ± 0.07	–0.30 ± 0.14
IRAS 23304+6147[a]	–0.79 ± 0.20	2.9 ± 0.3	1.55 ± 0.10	1.50 ± 0.09	1.52 ± 0.07	–0.05 ± 0.14
J004441.04-732136.4[c]	–1.34 ± 0.17	1.9 ± 0.7	2.06 ± 0.10	2.58 ± 0.10	2.40 ± 0.10	0.52 ± 0.10
J050632.10-714229.9[d]	–1.15 ± 0.17	1.5 ± 0.3	1.42 ± 0.07	1.07 ± 0.14	1.19 ± 0.09	–0.35 ± 0.15
J051213.81-693537.1[e]	–0.56 ± 0.15	1.3 ± 0.4	1.33 ± 0.08	1.74 ± 0.08	1.61 ± 0.06	0.41 ± 0.12
J051848.86-700246.9[e]	–1.03 ± 0.14	1.3 ± 0.3	1.46 ± 0.10	2.12 ± 0.08	1.90 ± 0.07	0.66 ± 0.13
J052043.86-692341.0[d]	–1.15 ± 0.17	1.6 ± 0.9	1.67 ± 0.12	1.85 ± 0.10	1.79 ± 0.08	0.19 ± 0.16
J053250.69-713925.8[d]	–1.22 ± 0.11	2.5 ± 0.7	1.51 ± 0.16	1.94 ± 0.10	1.80 ± 0.08	0.43 ± 0.19

Notes. [(a)] Galactic object, from Van Winckel & Reyniers (2000). For C/O, we assume an uncertainty of 0.3 dex. [(b)] Galactic object, from Reyniers et al. (2004). For C/O, we assume an uncertainty of 0.3 dex. [(c)] SMC object, from De Smedt et al. (2012). [(d)] LMC object, from van Aarle et al. (2013). [(e)] LMC object, from this paper.

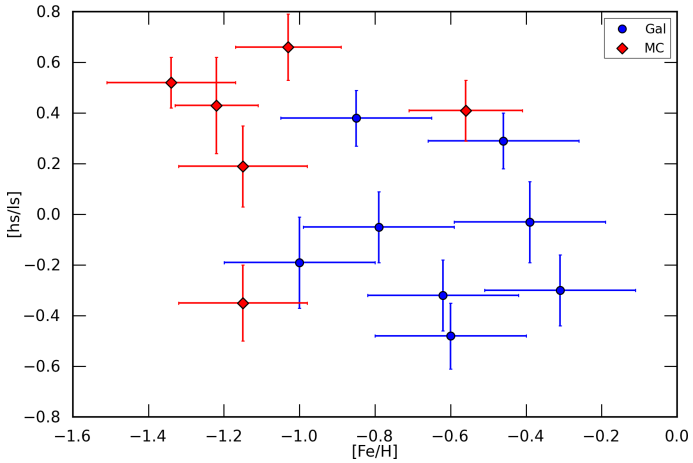

Fig. 13. Absence of correlation between the metallicity [Fe/H] and the [hs/ls] index for all stars listed in 7. Symbols are similar to Fig. 12. There is no clear correlation between metallicity and this range of metallicities.

[s/Fe] and [hs/ls] indices in Galactic and Magellanic Cloud objects, for which elements with high [s/Fe] generally show a higher [hs/ls] ratio. We add three objects (our two sample stars and J004441 from De Smedt et al. 2012) to this relation (see Fig. 12). We find that these three objects confirm the correlation between [s/Fe] and [hs/ls] with a correlation coefficient of 0.86. The [s/Fe] index represents the third dredge-up efficiency, although it is also influenced by the mass-loss history during the AGB phase and the envelope mass during TDUs. Note that the [hs/ls] index represents neutron irradiation, the number of neutrons that are available for each iron seed nucleus. Generally, an overabundance of hs-elements with respect to ls-elements is expected in low-mass and low-metallicity AGB stars (1−3 $M_{\odot}$) in which the $^{13}C(\alpha,n)^{16}O$ is expected to be the main neutron source for the *s*-process (e.g. Straniero et al. 1995; Gallino et al. 1998; Abia et al. 2002; Cristallo et al. 2011; Karakas & Lattanzio 2014). In heavier AGB stars, the $^{22}Ne(\alpha,n)^{25}Mg$ reaction is dominant, which mainly produces ls-elements. Of all the Magellanic Cloud objects listed in Table 7, all objects have low initial masses and an overabundance of hs with respect to ls, except for J050632.10-714229.9 (Fig. 11).

As described above, the [hs/ls] index is expected to increase with decreasing metallicity because of a larger number of neutrons for each iron seed, assuming that the diffusion of protons in the He-rich intershell is totally independent of metallicity. In Fig. 13, which also includes our sample stars and J004441, there is no clear correlation between [Fe/H] and [hs/ls].

Low-mass, low-metallicity stars are expected to have high overabundances of Pb with respect to the hs-elements. The AGB models predict the ^{13}C neutron source to be of primary origin, which means that it is independent of the initial metallicity. For similar models with different metallicity, the neutron production is predicted to be similar, but the number of available Fe seeds is different. Per Fe seed nucleus, there are more neutrons available at low metallicity. This results in the creation of heavier *s*-elements. Since Pb is the expected end-product of the *s*-process nucleosynthesis, high Pb abundances are expected in metal-poor stars.

In order to compare our Pb abundance results to mean theoretical predictions, we obtained predicted values from different AGB evolution and nucleosynthesis codes. For this comparison, we use [Pb/hs] ([Pb/Fe]−[hs/Fe]) and [Pb/ls] ([Pb/Fe]−[ls/Fe]), which represent the overabundance of Pb with respect to the other *s*-process elements. Figure 14 shows the comparison between the observed [Pb/hs] (upper panel) and [Pb/ls] (lower) upper limits, together with 2.0 $M_{\odot}$ model predictions of the STAREVOL code (Siess 2007, and references therein) for metallicities of [Fe/H] = −1.0, −0.5 and −0.2 dex (red full line), Mount-Stromlo Evolutionary code (MSE) predictions (Fishlock et al. 2014; Karakas 2010, and references therein) for [Fe/H] ≈ −1.3 and −0.15 dex for 2.0 $M_{\odot}$ models (black crosses) and [Fe/H] ≈ −0.5 dex for a 2.1 $M_{\odot}$ model (yellow diamond), and the publicly-available 2.0 $M_{\odot}$ model predictions of FRUITY (Cristallo et al. 2011) within a metallicity range from [Fe/H] = −1.5 up to 0.0 dex (blue point-dashed line) for seven different metallicities. Because of the limited number of available metallicities within the shown metallicity ranges, the STAREVOL and FRUITY curves in Fig. 14 are not smooth. We remark that, although all of the stars in Fig. 14 have estimated initial masses between 1.0 and 1.5 $M_{\odot}$ (see De Smedt et al. 2012; van Aarle et al. 2013, and Sect. 5.2), it is justified to make a comparison with 2.0 $M_{\odot}$ model predictions since the differences between the 1.5 and 2.0 $M_{\odot}$ FRUITY model predictions is only marginal.

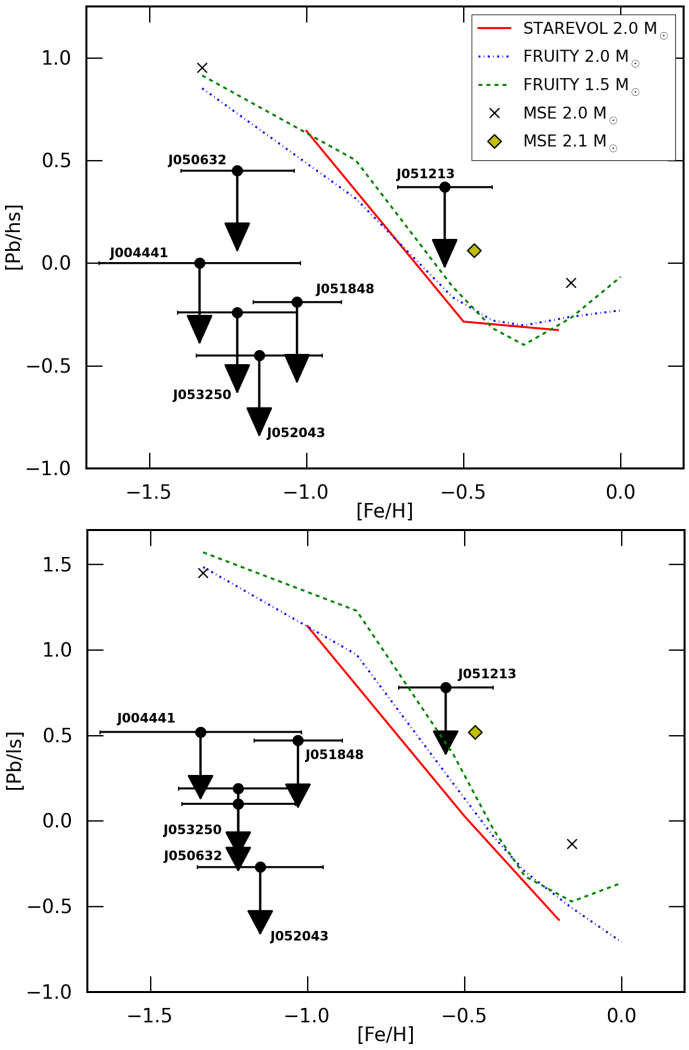

Fig. 14. Overview of the observed [Pb/hs] (*upper panel*) and [Pb/ls] (*lower panel*) upper limits of *s*-process enriched post-AGB stars in the Magellanic Clouds from this study and De Smedt et al. (2014). The observed abundance upper limits are plotted together with the [Pb/hs] and [Pb/ls] predictions of the 2.0 $M_{\odot}$ STAREVOL models (red full line),the 2.0 $M_{\odot}$ and 2.1 $M_{\odot}$ Mount Stromlo models (black crosses and yellow diamond, respectively) and the 1.5 and 2.0 $M_{\odot}$ FRUITY models (green dashed and blue dot-dashed lines, respectively). The black horizontal lines represent the [Fe/H] uncertainty of the stars shown. The position of each star is indicated with the first part of its 2MASS name. For more information, see text.

Figure 14 shows that the predictions fit well the observed Pb abundance upper limit of J051213 but strongly overestimate the Pb overabundances of the lower metallicity stars. There is an increasing discrepancy between predicted and observed Pb abundances towards lower metallicities. A larger sample of post-AGB stars with derived Pb abundances is required to confirm the observed discrepancy towards lower metallicities. More research is clearly needed to explain the consistent low Pb abundances in *s*-process enriched low-metallicity post-AGB stars. This is beyond the scope of this study.

7. Conclusions

We aim to understand the chemical diversity demonstrated by post-AGB stars, and we focus on *s*-process rich objects. With detailed studies of a well-sampled grid of post-AGB objects covering a wide range in luminosity (hence core-mass and initial mass) and metallicity, we aim to build up a systematic set of constraints on AGB models. These will help us to understand the physical processes related to AGB nucleosynthesis and mixing. To obtain these constraints, we study newly discovered post-AGB stars in the Magellanic Clouds. Because of their known distances, accurate luminosity and, hence, initial mass estimates can be made, which is contrary to the situation for Galactic peers.

Here, we report on a detailed chemical study of two *s*-process enriched optically visible post-AGB stars in the LMC. The objects were carefully selected from our low-resolution surveys (van Aarle et al. 2011; Kamath et al. 2015). Our high-resolution spectral data reveal very rich spectra, literally swamped with atomic lines of *s*-process elements. We quantified that both objects belong to the most *s*-process rich objects known to date despite their similarly low C/O ratios. The metallicity difference between both stars is about 0.5 dex.

With the addition of our two sample stars, all *s*-process enhanced post-AGB stars in the LMC and SMC studied thus far cluster in the same region of the HR-diagram. All are associated with the latest evolutionary phase of low-mass stars with, on average, low metallicity.

We also confirm the correlation between [hs/ls] and [s/Fe] for *s*-process enriched post-AGB stars and find that both Galactic and Magellanic Cloud objects follow the same relation. The neutron exposure as traced by [hs/ls] is correlated with the overall *s*-process overabundances, as traced by [s/Fe]. [s/Fe] is also determined by the amount of dredged-up intershell material and the envelope dilution. In addition, we strengthen and confirm that there is no clear correlation between neutron irradiation and metallicity. Furthermore, we find an increasing discrepancy between observed and predicted Pb overabundances towards lower metallicities: the higher metallicity J051213 with [Fe/H] ≈ -0.56 dex fits well the model predictions, while J051848 and other Magellanic Cloud objects from previous studies reveal much lower [Pb/hs] and [Pb/ls] results than predicted.

Our current and future research involves expanding our survey of chemical studies in the Magellanic Clouds to construct a grid that cover a larger and well-sampled range in luminosity (hence initial mass) and metallicity. We intend to use this grid of constraints to fine-tune AGB models and therefore the underlying physics of nucleosynthesis and mixing.

Acknowledgements. The authors thank the referee Claudio B. Pereira for the constructive comments that improved the quality of this paper. The authors thank L. Siess, S. Goriely for providing the STAREVOL Pb abundance predictions. The authors thank A.I. Karakas for providing the Mount Stromlo Pb abundance predictions. K.D.S., H.V.W., and D.K. acknowledge support of the KU Leuven contract GOA/13/012. D.K. acknowledges support of the FWO grant G.OB86.13.

References

Abia, C., Domínguez, I., Gallino, R., et al. 2002, ApJ, 579, 817
Abia, C., de Laverny, P., & Wahlin, R. 2008, A&A, 481, 161
Asplund, M., Grevesse, N., Sauval, A. J., & Scott, P. 2009, ARA&A, 47, 481
Busso, M., Lambert, D. L., Beglio, L., et al. 1995, ApJ, 446, 775
Cardelli, J. A., Clayton, G. C., & Mathis, J. S. 1989, ApJ, 345, 245
Castelli, F., & Kurucz, R. L. 2003, Modelling of Stellar Atmospheres, eds. N. Piskunov et al., IAU Symp., 210, A20
Cristallo, S., Piersanti, L., Straniero, O., et al. 2011, ApJS, 197, 17
Cutri, R. M., Skrutskie, M. F., van Dyk, S., et al. 2003, VizieR Online Data Catalog: II/246
Cutri, R. M., Wright, E. L., Conrow, T., et al. 2012, Explanatory Supplement to the WISE All-Sky Data Release Products, Tech. Rep.
Dekker, H., D'Odorico, S., Kaufer, A., Delabre, B., & Kotzlowski, H. 2000, in SPIE Conf. Ser. 4008, eds. M. Iye, & A. F. Moorwood, 534

Deroo, P., Reyniers, M., Van Winckel, H., Goriely, S., & Siess, L. 2005, A&A, 438, 987
De Smedt, K., Van Winckel, H., Karakas, A. I., et al. 2012, A&A, 541, A67
De Smedt, K., Van Winckel, H., Kamath, D., et al. 2014, A&A, 563, L5
Fishlock, C. K., Karakas, A. I., Lugaro, M., & Yong, D. 2014, ApJ, 797, 44
Fouqué, P., Chevallier, L., Cohen, M., et al. 2000, A&AS, 141, 313
Gallino, R., Arlandini, C., Busso, M., et al. 1998, ApJ, 497, 388
Geisler, D., Grocholski, A., Sarajedini, A., Cole, A., & Smith, V. 2009, in LMC Cluster Abundances and Kinematics, eds. T. Richtler, & S. Larsen, 133
Kamath, D., Wood, P. R., & Van Winckel, H. 2014, MNRAS, 439, 2211
Kamath, D., Wood, P. R., & Van Winckel, H. 2015, MNRAS, 454, 1468
Karakas, A. I. 2010, MNRAS, 403, 1413
Karakas, A. I., & Lattanzio, J. C. 2014, PASA, 31, 30
Keller, S. C., & Wood, P. R. 2006, ApJ, 642, 834
Kiselman, D. 2002, in Highlights of Astronomy, 12, 429
Kobayashi, C., Karakas, A. I., & Umeda, H. 2011, MNRAS, 414, 3231
Kupka, F., Piskunov, N., Ryabchikova, T. A., Stempels, H. C., & Weiss, W. W. 1999, A&AS, 138, 119
Lapenna, E., Mucciarelli, A., Origlia, L., & Ferraro, F. R. 2012, ApJ, 761, 33
Luck, R. E., Moffett, T. J., Barnes, III, T. G., & Gieren, W. P. 1998, AJ, 115, 605
Massey, P. 2002, ApJS, 141, 81
Meixner, M., Gordon, K. D., Indebetouw, R., et al. 2006, AJ, 132, 2268
Pompéia, L., Hill, V., Spite, M., et al. 2008, A&A, 480, 379
Rao, S. S., Giridhar, S., & Lambert, D. L. 2012, MNRAS, 419, 1254
Reid, W. A., & Parker, Q. A. 2010, MNRAS, 405, 1349
Reyniers, M., Van Winckel, H., Gallino, R., & Straniero, O. 2004, A&A, 417, 269
Romano, D., Karakas, A. I., Tosi, M., & Matteucci, F. 2010, A&A, 522, A32
Schlegel, D. J., Finkbeiner, D. P., & Davis, M. 1998, ApJ, 500, 525
Siess, L. 2007, A&A, 476, 893
Sneden, C. A. 1973, Ph.D. Thesis, The University of Texas at Austin
Storm, J., Gieren, W., Fouqué, P., et al. 2011, A&A, 534, A95
Straniero, O., Gallino, R., Busso, M., et al. 1995, ApJ, 440, L85
van Aarle, E., van Winckel, H., Lloyd Evans, T., et al. 2011, A&A, 530, A90
van Aarle, E., Van Winckel, H., De Smedt, K., Kamath, D., & Wood, P. R. 2013, A&A, 554, A106
van der Marel, R. P., Alves, D. R., Hardy, E., & Suntzeff, N. B. 2002, AJ, 124, 2639
Van der Swaelmen, M., Hill, V., Primas, F., & Cole, A. A. 2013, A&A, 560, A44
Van Winckel, H. 2003, ARA&A, 41, 391
Van Winckel, H., & Reyniers, M. 2000, A&A, 354, 135
Vassiliadis, E., & Wood, P. R. 1994, ApJS, 92, 125